Supplementary Information

Molecular mechanisms of CAND2 in regulating SCF ubiquitin ligases

Kankan Wang[1], Lihong Li[1,2], Sebastian Kenny[3], Dailin Gan[4], Justin M. Reitsma[5,6], Yun Zhou[2,7], Chittaranjan Das[3], and Xing Liu[1,2*]

* Correspondence to: xingliu@purdue.edu

Supplementary Figure 1. CAND2 is homologous to CAND1.

Sequence alignment and secondary structure analyses of CAND1 and CAND2. The blue box highlights the conserved β hairpin region.

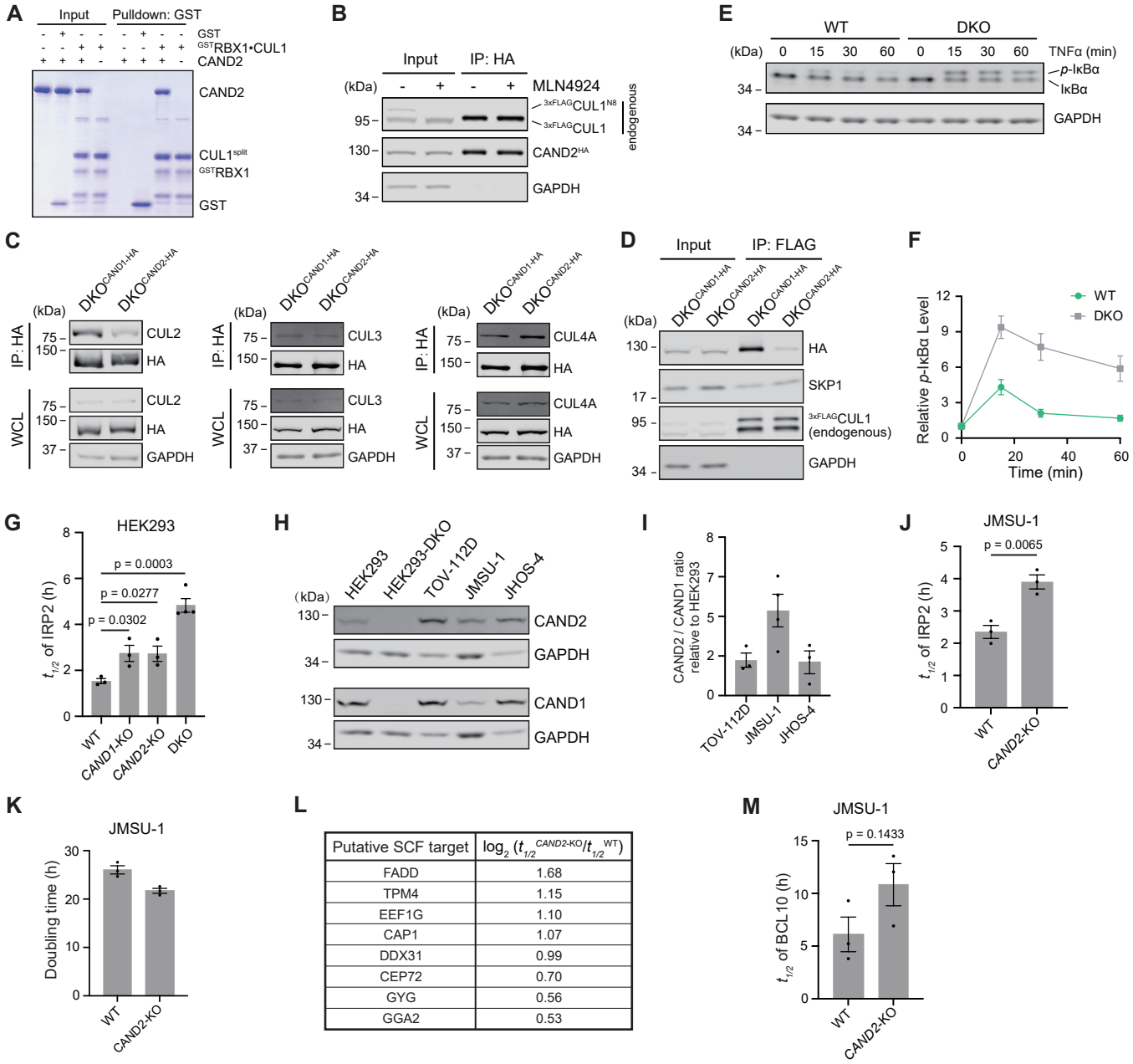

Putative SCF target	$\log_2 (t_{1/2}^{CAND2\text{-}KO}/t_{1/2}^{WT})$
FADD	1.68
TPM4	1.15
EEF1G	1.10
CAP1	1.07
DDX31	0.99
CEP72	0.70
GYG	0.56
GGA2	0.53

Supplementary Figure 2. CAND2 binds cullins and modulates protein degradation.

(**A**) A GST pulldown assay was used to evaluate the interaction between CUL1 and CAND2. The indicated recombinant proteins were mixed and incubated with GST beads. The samples were analyzed by SDS–PAGE and Coomassie blue staining. Representative results from two independent experiments are shown.

(**B**) CAND2 prefers to bind unneddylated CUL1. DKO cells expressing endogenous ^{3xFLAG}CUL1 were induced to express CAND2^{HA}. Cells were treated with or without 1 μM MLN4924 for 1 h before harvesting. Whole-cell lysates were immunoprecipitated with an anti-HA antibody followed by immunoblotting with anti-FLAG, anti-HA and anti-GAPDH antibodies. Representative results from three independent experiments are shown.

(**C**) CAND2 binds to multiple cullins in human cell lysates (related to Figure 1A). Whole-cell lysate (WCL) from HEK293 cells of the indicated genotypes were immunoprecipitated (IP) with an anti-HA antibody. Cells were treated with 1 μM MLN4924 for 1 h before harvesting. Samples were immunoblotted with anti-CUL2, anti-CUL3, anti-CUL4A, anti-HA, and anti-GAPDH antibodies. Representative results from three independent experiments are shown.

(**D**) CAND2 binds CUL1 less efficiently than CAND1 in human cell lysates. $CAND1^{HA}$ or $CAND2^{HA}$ was expressed at equal levels in DKO cells expressing endogenous ^{3xFLAG}CUL1. Whole-cell lysates were immunoprecipitated with an anti-FLAG antibody in the presence of the $CUL1^{split}$•RBX1 "sponge" protein, MLN4924, and quinoline-8-thiol (8TQ). The samples were immunoblotted with the indicated antibodies. Representative results from three independent experiments are shown.

(**E-F**) TNFα-induced degradation of *p*-IκBα is impaired in DKO HEK293 cells (related to Figure 1B-C). (**E**) Immunoblotting of IκBα and GAPDH at the indicated time points after the addition of TNFα to the indicated cells in the presence of cycloheximide (CHX). (**F**) Relative levels of *p*-IκBα in (E). Data are presented as mean ± SEM; n = 3 independent experiments.

(**G**) Half-lives of IRP2 in response to FAC in the indicated HEK293 cells. Data from Figure 1E were individually fit to a single-exponential decay model to estimate $t_{1/2}$ for each replicate. Values are presented as mean ± SEM; n = 3 independent experiments except for DKO (n = 4). Unpaired two-tailed Student's *t*-test.

(**H-I**) The ratio of CAND2 to CAND1 protein levels is higher in JMSU-1 cells than in HEK293 cells. (**H**) Immunoblotting of CAND2 and CAND1 in indicated cell lines. (**I**) Ratios of CAND2 to CAND1 protein levels were quantified and normalized to that of HEK293 cells. Data are presented as mean ± SEM; n = 3 independent experiments except for JMSU-1 (n = 4).

(**J**) Half-lives of IRP2 in response to FAC in the indicated JMSU-1 cells. Data from Figure 2C were individually fit to a single-exponential decay model to estimate $t_{1/2}$ for each replicate. Values are presented as mean ± SEM; n = 3 independent experiments. Unpaired two-tailed Student's *t*-test.

(**K**) Doubling time of WT and *CAND2*-KO JMSU-1 cells. Data are presented as mean ± SEM; n = 3 independent experiments.

(**L**) The global protein turnover assay identified putative SCF targets that exhibit longer half-lives upon *CAND2*-KO in JMSU-1 cells (related to Figure 2E).

(**M**) Half-lives of BCL10 in the indicated JMSU-1 cells. Data from Figure 2H were individually fit to a single-exponential decay model to estimate $t_{1/2}$ for each replicate. Values are presented as mean ± SEM; n = 3 independent experiments. Unpaired two-tailed Student's *t*-test. Source data are provided in the Source Data file.

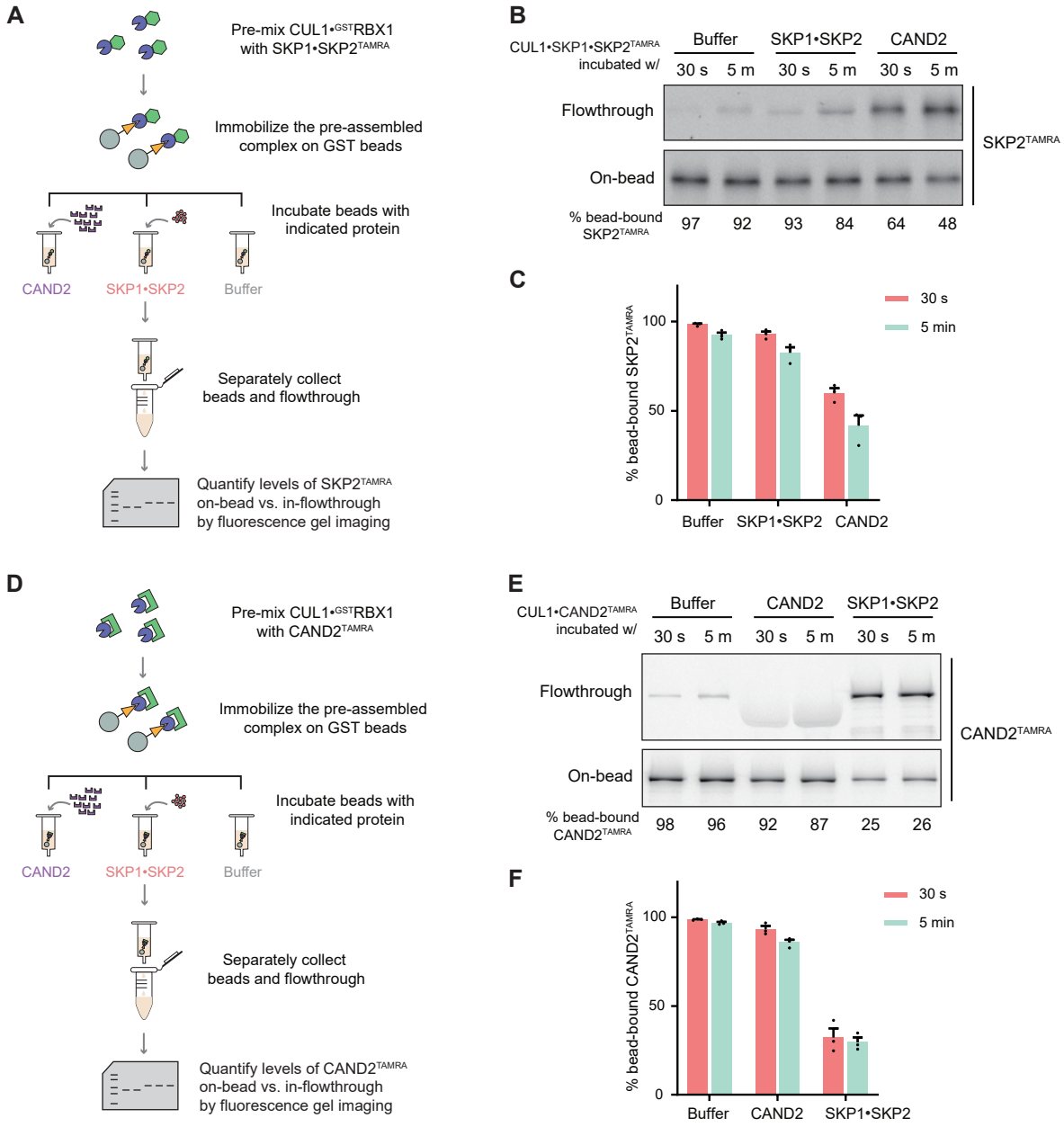

Supplementary Figure 3. CAND2 promotes FBP exchange.

(**A-C**) CAND2 accelerates SCF^{SKP2} disassembly *in vitro*. (**A**) Schematic illustration of the experimental design. Pre-mixed 0.2 μM CUL1•^{GST}RBX1 and SKP1•$SKP2^{TAMRA}$ were immobilized on GST beads and incubated with buffer, or 2 μM SKP1•SKP2, or 2 μM CAND2, for 30 s or 5 min before the beads and flowthrough were separated. The levels of $SKP2^{TAMRA}$ on-bead vs. in-flowthrough were determined by fluorescence gel imaging. (**B**) A representative result of (A). (**C**) Percentage of $SKP2^{TAMRA}$ that remained associated with bead-bound CUL1•^{GST}RBX1. Data are presented as mean ± SEM; n = 3 independent experiments.

(**D-F**) SKP1•SKP2 accelerates CUL1•CAND2 disassembly *in vitro*. (**D**) Schematic illustration of the experimental design, which is similar to that in (A) except that pre-mixed 0.2 μM CUL1•^{GST}RBX1 and $CAND2^{TAMRA}$ were immobilized on GST beads. (**E**) Samples from (A) were subjected to SDS–PAGE and fluorescence scanning. (**F**) Percentage of $CAND2^{TAMRA}$ that remained associated with bead-bound CUL1•^{GST}RBX1. Data are presented as mean ± SEM; n = 3 independent experiments. Source data are provided as a Source Data file.

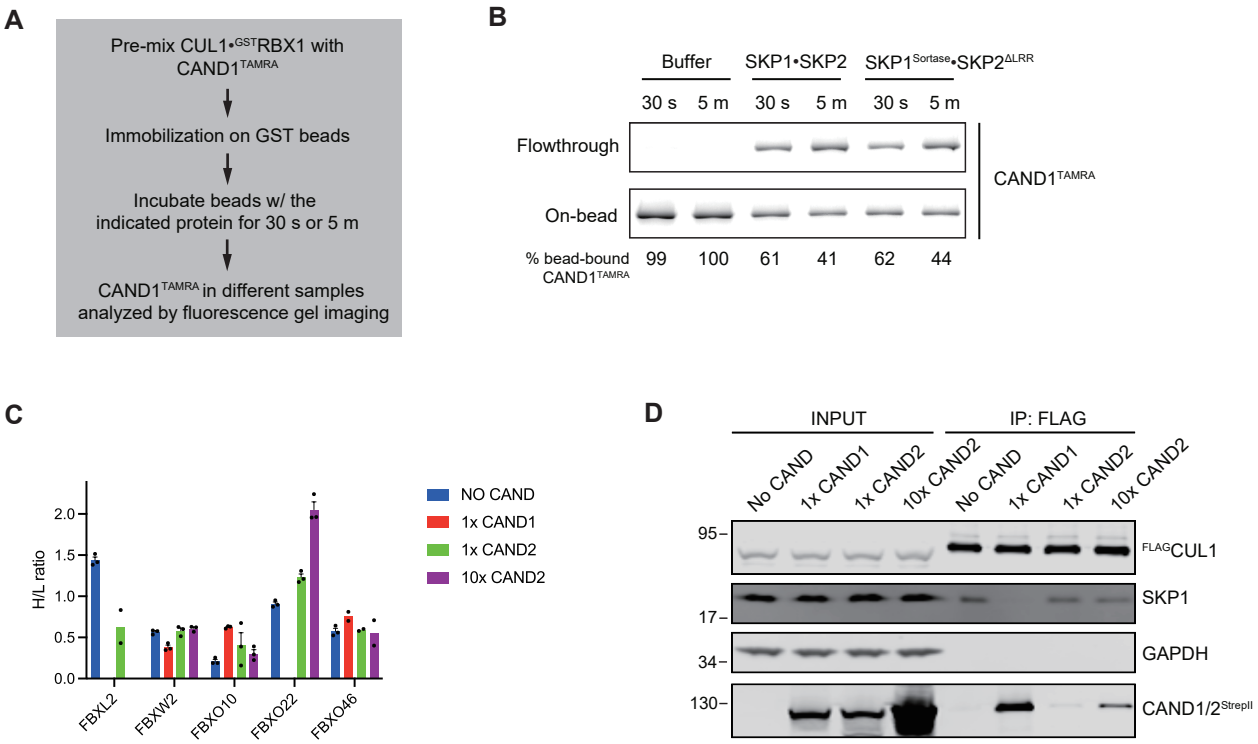

Supplementary Figure 4. FBP exchange in response to CAND1 vs. CAND2.

(**A-B**) SKP1^{Sortase}•SKP2$^{\Delta LRR}$ is equivalent to SKP1•SKP2 in its ability to dissociate CAND1 from CUL1. (**A**) Schematic illustration of the experimental design. Pre-mixed 0.2 μM CUL1•^{GST}RBX1 and CAND1^{TAMRA} were immobilized on GST beads and incubated with buffer, or 2 μM SKP1•SKP2, or 2 μM SKP1^{Sortase}•SKP2$^{\Delta LRR}$, for 30 s or 5 min before the beads and flowthrough were separated. The levels of CAND1^{TAMRA} on-bead vs. in-flowthrough were determined via fluorescence gel imaging. (**B**) Representative results of (A) from two independent experiments are shown.

(**C**) Exchange levels of FBPs that showed atypical responses to CAND1 and/or CAND2 (related to Figure 3). Results from three biological replicates are shown. Data are presented as mean ± SEM; n = 3 biological replicates except for FBXL2 in the 1× CAND2 group and FBXO46 in the 1× CAND1, 1× CAND2 and 10× CAND2 groups (n = 2 biological replicates).

(**D**) Immunoblotting of samples prepared for mass spectrometry as described in Figure 3C. Representative results from three biological replicates are shown. Source data are provided as a Source Data file.

Supplementary Figure 5

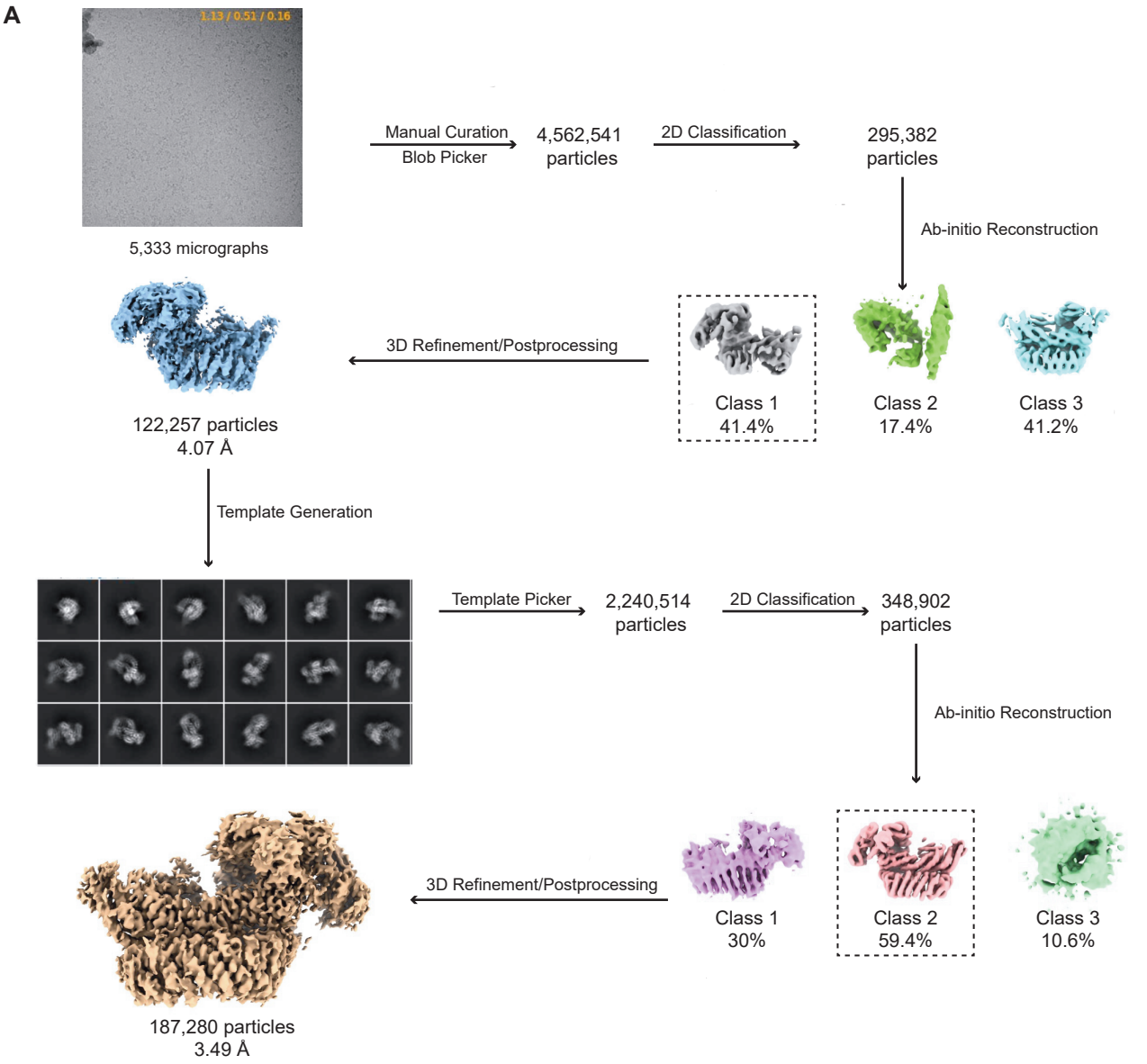

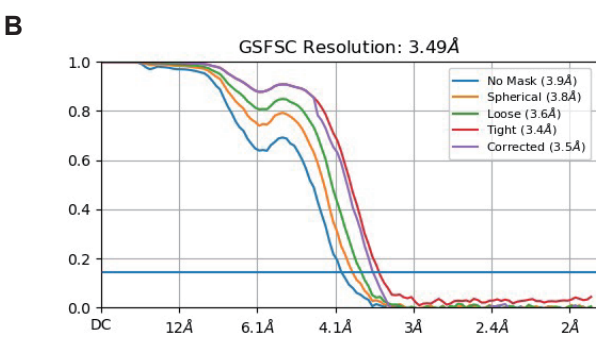

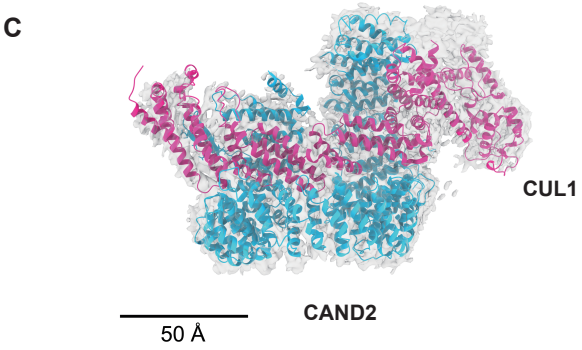

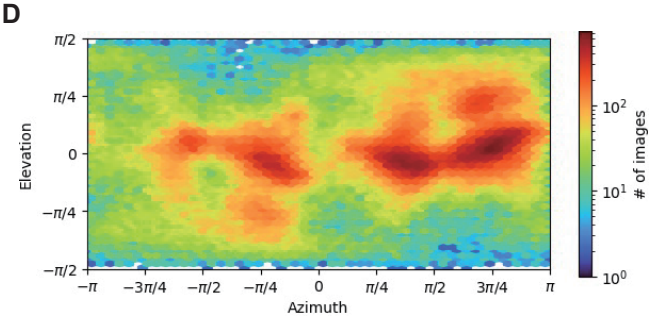

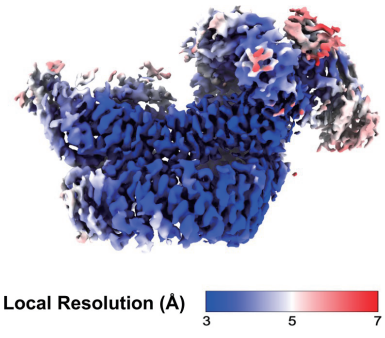

Supplementary Figure 5. Cryo-EM data analysis and structure determination (related to Figure 5).

(**A**) Procedure of cryo-EM data processing for the CUL1•CAND2 complex performed in CryoSparc.

(**B**) Gold-standard Fourier shell correlation (GSFSC) curves of the final 3D reconstructions. The blue line intercepts the y-axis at an FSC value of 0.143.

(**C**) View of the CUL1•CAND2 model in the final map.

(**D**) Angular distribution of the particles used for the final reconstruction.

(**E**) Local resolution estimation of the final reconstruction.

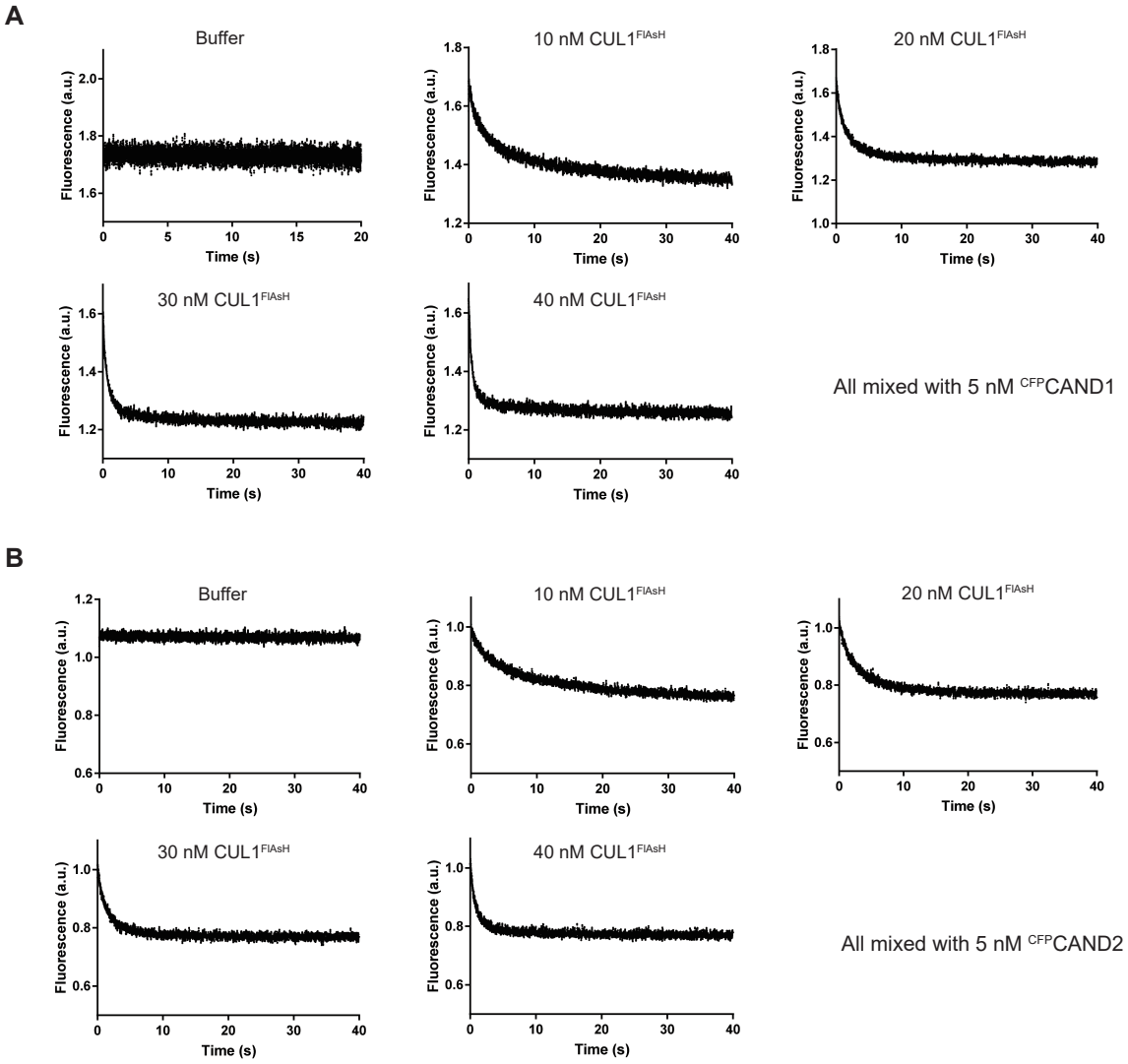

Supplementary Figure 6. Measurements of the k_{on} of CUL1•CAND1 and CUL1•CAND2 (related to Figure 6D).

(**A**) Real-time CFP signals upon mixing the indicated concentrations of CUL1^{FlAsH} with 5 nM ^{CFP}CAND1 in a stopped-flow apparatus. The signal changes were fit to a one-phase exponential model to obtain the k_{obs}.

(**B**) Same as in (A) except that ^{CFP}CAND1 was replaced by ^{CFP}CAND2. Source data are provided in the Source Data file.

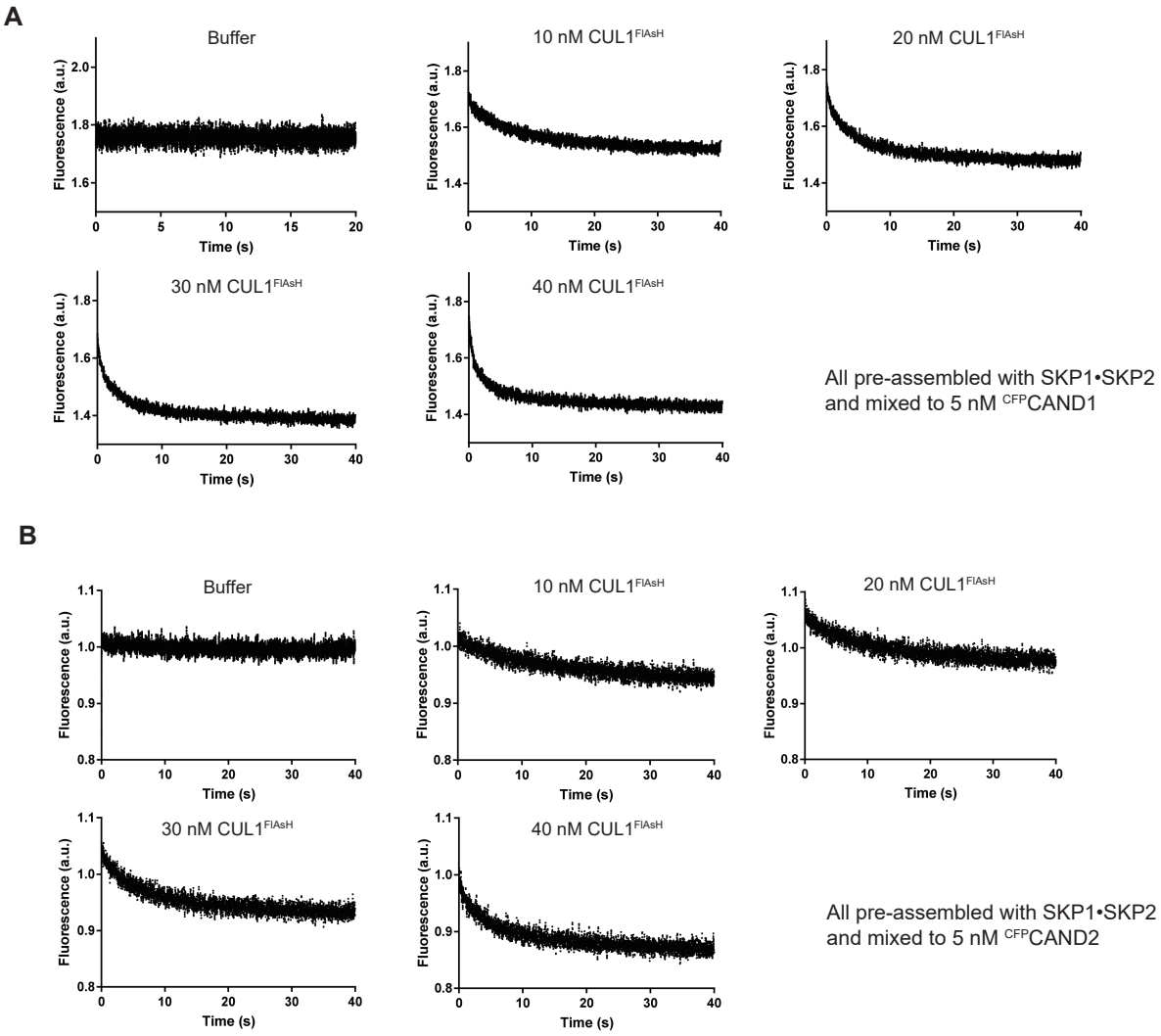

Supplementary Figure 7. Measurements of the k_{on} of CUL1•CAND1 and CUL1•CAND2 in the presence of SKP1•SKP2 (related to Figure 7A).

(**A**) Real-time CFP signals upon mixing 5 nM ^{CFP}CAND1 with the indicated concentrations of CUL1^{FlAsH} preassembled with SKP1•SKP2 in a stopped-flow apparatus. The signal changes were fit to a one-phase exponential model to obtain the k_{obs}.

(**B**) Same as in (A) except that ^{CFP}CAND1 was replaced by ^{CFP}CAND2. Source data are provided in the Source Data file.

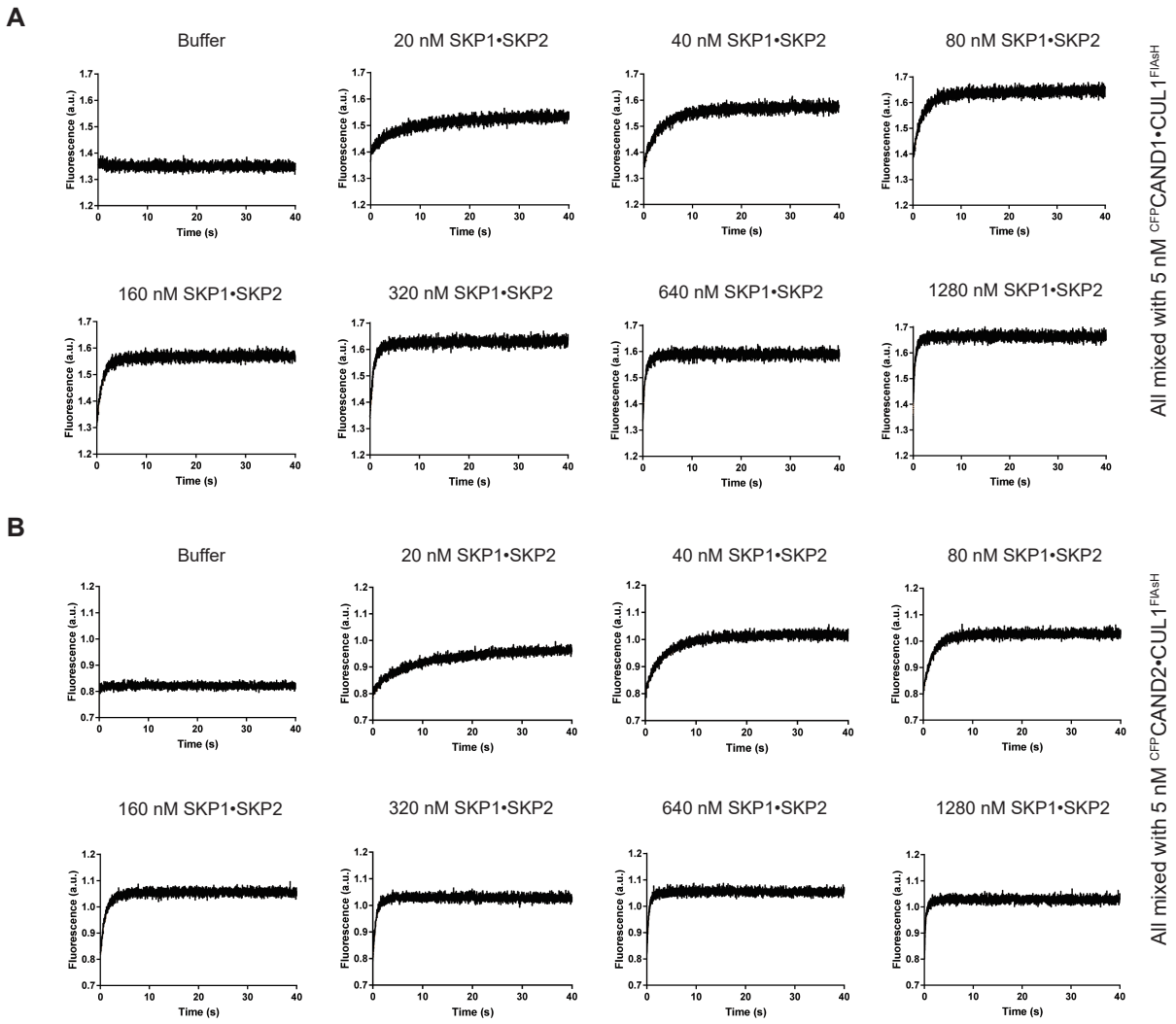

Supplementary Figure 8. Measurements of the k_{off} of CUL1•CAND1 and CUL1•CAND2 in the presence of SKP1•SKP2 (related to Figure 7D).

(**A**) Real-time CFP signals upon mixing the indicated concentrations of SKP1•SKP2 with 5 nM preassembled ^{CFP}CAND1•CUL1^{FlAsH} in a stopped-flow apparatus. The signal changes were fit to a one-phase exponential model to obtain the k_{obs}.

(**B**) Same as in (A) except that ^{CFP}CAND1•CUL1^{FlAsH} was replaced by ^{CFP}CAND2•CUL1^{FlAsH}. Source data are provided in the Source Data file.

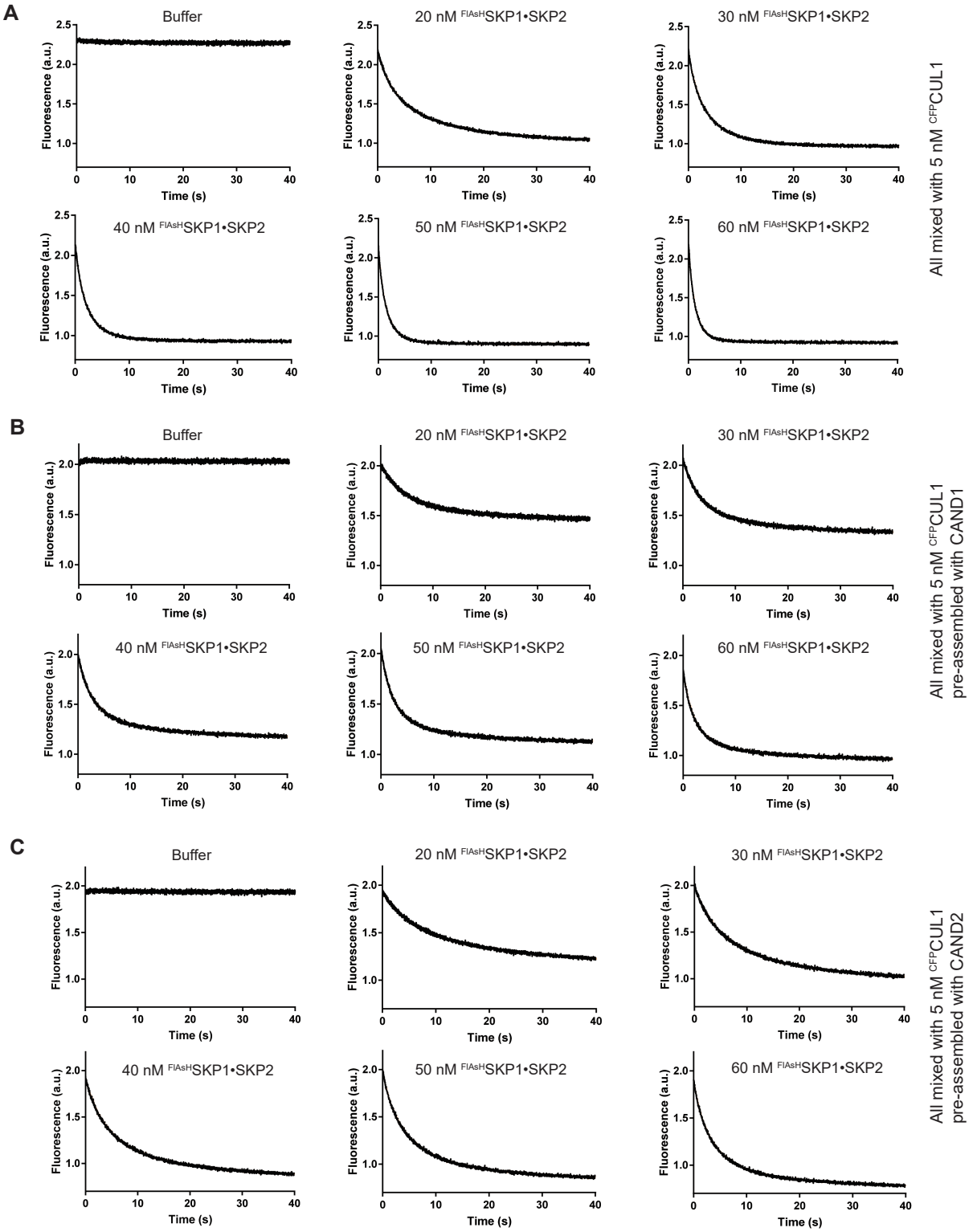

Supplementary Figure 9. Measurements of the k_{on} of SCF^{SKP2} in the absence and presence of CAND1 or CAND2 (related to Figure 8B).

(**A**) Real-time CFP signals upon mixing the indicated concentrations of ^{FlAsH}SKP1•SKP2 with 5 nM ^{CFP}CUL1 in a stopped-flow apparatus. The signal changes were fit to a one-phase exponential model to obtain the k_{obs}.

(**B**) Same as in (A) except that the 5 nM ^{CFP}CUL1 was preincubated with 20 nM CAND1.

(**C**) Same as in (B) except that the 20 nM CAND1 was replaced with 20 nM CAND2. Source data are provided in the Source Data file.

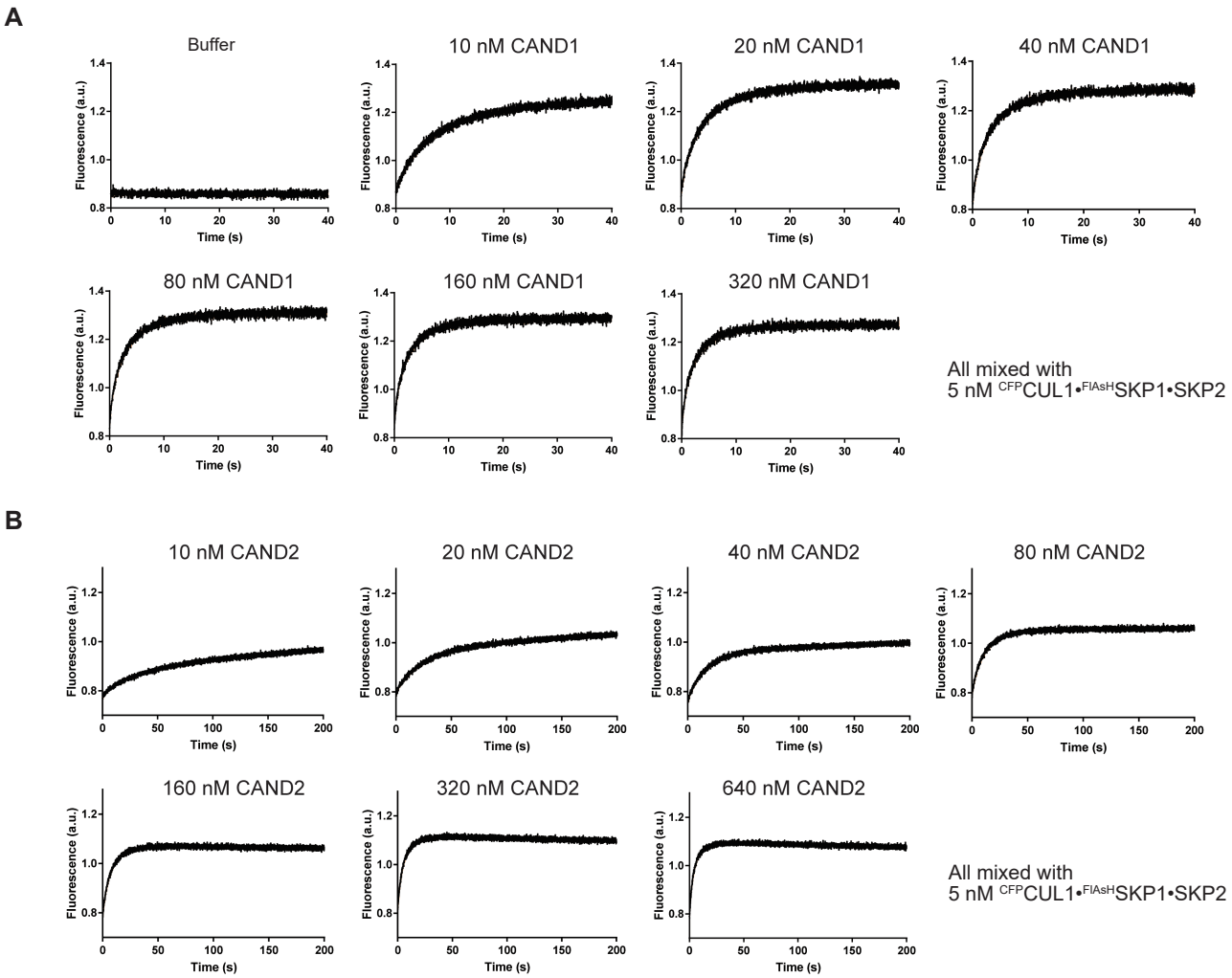

Supplementary Figure 10. Measurements of the k_{off} of SCF^{SKP2} in the presence of CAND1 or CAND2 (related to Figure 8D).

(**A**) Real-time CFP signals upon mixing the indicated concentrations of CAND1 with 5 nM preassembled ^{CFP}CUL1•^{FlAsH}SKP1•SKP2 in a stopped-flow apparatus. The signal changes were fit to a one-phase exponential model to obtain the k_{obs}.

(**B**) Same as in (A) except that CAND1 was replaced with CAND2. Source data are provided in the Source Data file.

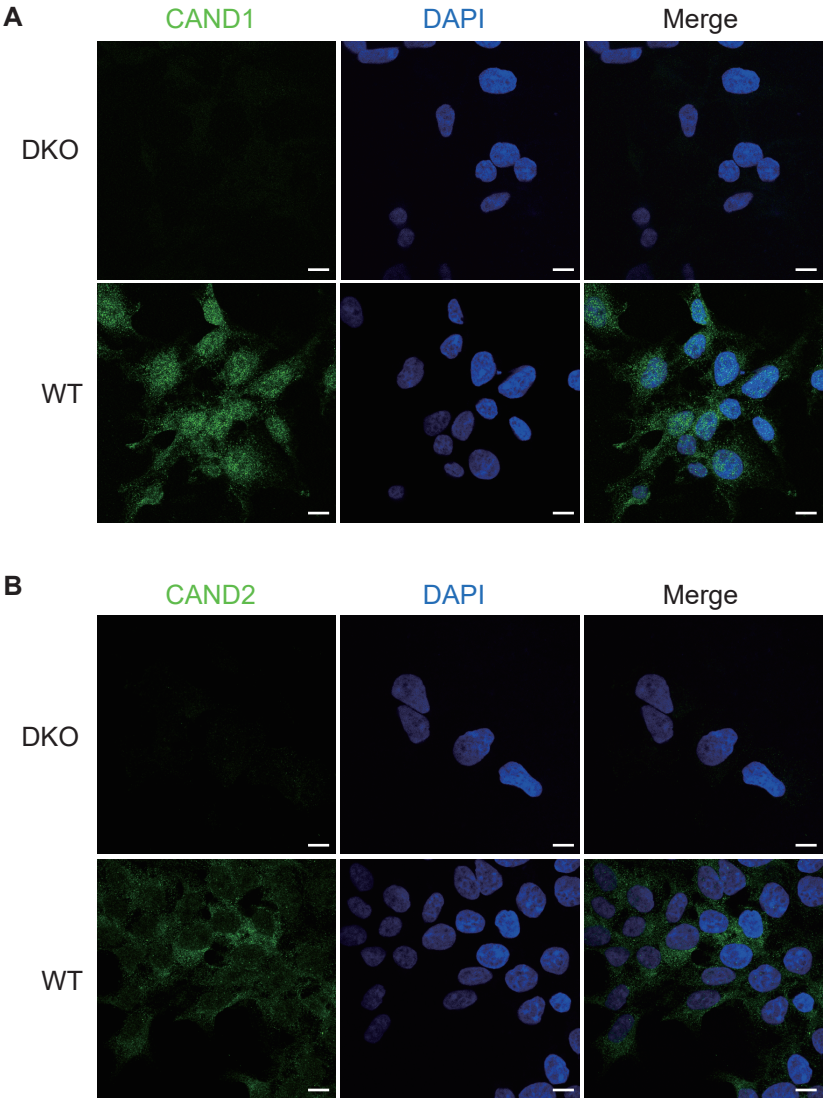

Supplementary Figure 11. Localization of CAND1 and CAND2 in HEK293 cells.

Immunofluorescence analysis of CAND1 (**A**) and CAND2 (**B**) in WT HEK293 cells, with DKO cells serving as negative controls. Both WT and DKO cells were processed and imaged under identical conditions. The results closely match those reported in the Human Protein Atlas, with the same anti-CAND1 and anti-CAND2 antibodies used as in the Human Protein Atlas. Scale bar: 10 μm. Representative results from two independent experiments are shown.

Supplementary Table 1. Cryo-EM data collection, refinement and validation statistics

	CUL1•CAND2 complex (EMD-43572) (PDB 8VVY)
Data collection and processing	
Magnification	105,000x
Voltage (kV)	300
Electron exposure (e–/Å^2)	51.2
Defocus range (μm)	1.0-3.0
Pixel size (Å)	0.95
Symmetry imposed	C1
Initial particle images (no.)	4562541
Final particle images (no.)	187280
Map resolution (Å)	3.49
FSC threshold	0.143
Map resolution range (Å)	3.0-7.0
Refinement	
Initial model used	AlphaFold (AF-O75155-F1 and AF-Q13616-F1)
Map sharpening *B* factor (Å^2)	204.8
Model composition	
Non-hydrogen atoms	14953
Protein residues	1901
Ligands	0
B factors (Å^2)	
Protein	90.09
Ligand	---
R.m.s. deviations	
Bond lengths (Å)	0.003
Bond angles (°)	0.608
Validation	
MolProbity score	1.76
Clashscore	8.1
Poor rotamers (%)	0
Ramachandran plot	
Favored (%)	95.4
Allowed (%)	4.55
Disallowed (%)	0.05

Note: RBX1 is present in the complex but not modeled.